# Welding of Iron Aluminides

*The weldability of $Fe_3Al$ is very sensitive to the welding conditions and alloy content conditions*

BY S. A. DAVID, J. A. HORTON, C. G. McKAMEY, T. ZACHARIA AND R. W. REED

ABSTRACT. Ordered intermetallic alloys, such as iron aluminides, are a unique class of metallic materials which form long-range-ordered crystal structures below their melting points ($T_m$) or critical ordering temperatures ($T_c$). Iron aluminides, which are brittle at room temperature, have been ductilized at Oak Ridge National Laboratory using physical metallurgy principles. A key issue in the development of these alloys for engineering applications is weldability.

An investigation was carried out to determine the weldability of a class of binary and higher order iron aluminides. Thin sheets of iron aluminides were gas tungsten arc and electron beam welded at different travel speeds and power levels. The results indicate that the weldability of these alloys is very sensitive to the welding conditions, producing good welds sometimes and severely cracked welds at other times. Alloys containing $TiB_2$ additions for improved strength and ductility cracked severely upon welding. The results of the hot ductility tests show that the modified iron aluminide alloys are very ductile at elevated temperatures and show no evidence of heat-affected zone (HAZ) cracking.

## Introduction

The ordered intermetallic alloys are a unique class of materials with an atomic arrangement distinctly different from that of conventional or disordered alloys. Below the melting point ($T_m$) or critical ordering temperature ($T_c$) the various atomic species in these alloys tend to occupy specific sublattice sites and form superlattice structures. In the 1950's and the 1960's, the structures and properties of these ordered intermetallics were investigated extensively and as a result many attractive properties were identified (Refs. 1-4). The superior performance of these alloys is associated with the relatively slow atomic mobility and unique dislocation dynamics in ordered lattices. However, their tendency to be brittle in the ordered state has limited their use for structural applications. Liu and others (Refs. 5-12) have shown that ductility and fabricability of several intermetallic alloys can be substantially improved using physical metallurgy principles.

Of the various ordered intermetallic alloys, an alloy of recent interest is the iron aluminide, $Fe_3Al$. $Fe_3Al$ can occur in any of the three different kinds of crystal structure depending on the temperature: an ordered $DO_3$-type superlattice structure below $\approx 550°C$, an ordered B2-type superlattice between 550° and $\approx 750°C$ (1022° and 1382°F), and disordered bcc at higher temperatures. The B2-type structure is basically bcc, while $DO_3$ is comprised of eight bcc cells stacked two deep in each direction and results in the same symmetry as an fcc structure. Figure 1 shows the phase diagram of the iron-rich region of the Fe-Al system (Refs. 13, 14). At room temperature, alloys with less than $\approx 18.5$ at.-% Al are bcc solid solution with a disordered structure. However, alloys with 18.5–35.0 at.-% Al form a $DO_3$ structure. Alloys with greater than $\approx 35$ at.-% Al form the cubic FeAl B2-type ordered structure.

Iron aluminide also has attractive electrical, magnetic and corrosion-resistance properties. Other features, such as the low cost of iron and aluminum, and low density and adequate strength at temperatures below 600°C (1112°F), make iron aluminides attractive candidates for structural applications. However, lack of ductility at room temperature and a sharp reduction in strength above 600°C are major obstacles in their utilization as structural materials. Earlier studies have shown that increasing the purity of $Fe_3Al$ shifted the failure mode from intergranular to transgranular (Refs. 15, 16). Various investigations with ternary additions have also been carried out to improve ductility (Refs. 17–21).

One of the major issues in the development of this new class of material, including $Fe_3Al$, is welding, because joining by conventional welding is an important means of fabricating engineering materials into structural components. This paper describes the behavior of $Fe_3Al$-based alloys when subjected to weld thermal cycles. Weldability of these alloys using electron beam (EB) and gas tungsten arc (GTA) welding processes will be described. In addition, microstructural characteristics of $Fe_3Al$ alloy welds and the effects of alloying additions on the weldability will be described.

**KEY WORDS**

Aluminide Weldability
Iron Aluminides
Aluminides Made Ductile
$TiB_2$ Additions
GTAW of Aluminides
EBW for Aluminides
Intermetallic Alloys
Ordered Structures
Aluminide Cracking
Hot Cracks

## Experimental Procedure

The alloys used in this study are listed in Table 1. The alloys were prepared by arc melting under argon and drop casting into water-cooled copper molds. After homogenization for 5 h at 1000°C (1832°F), the alloys were hot-rolled to a final thickness of 0.76 mm (0.03 in.) starting at 1000°C and finishing at 600°C. They were then annealed 1 h at 850°C (1562°F) for recrystallization and at 500°C (932°F) for 5 days to produce the $DO_3$ order. Both EB and GTA autogenous welds were made on 20 × 40 × 0.7-mm (0.79 × 1.6 × 0.03-in.) coupons. The welding variables were adjusted to produce full-penetration welds at various welding speeds. The welding variables used to produce full-penetration EB welds were: welding speed 4.2 to 16.9 mm/s (0.16 to 0.66 in./s); accelerating voltage, 75 kV; and beam current, 2.5 to 5.5 mA. Full-penetration GTA welds were produced using a welding current of 35 to 45 A and welding speeds ranging from

*S. A. DAVID, J. A. HORTON, C. G. McKAMEY, T. ZACHARIA and R. W. REED are with the Metals and Ceramics Division, Oak Ridge National Laboratory, Oak Ridge, Tenn.*

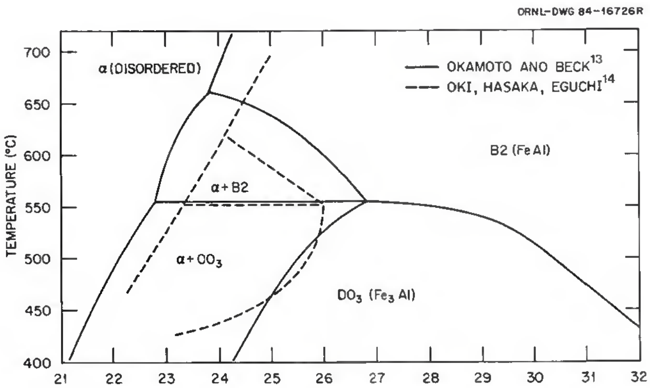


*Fig. 1—The iron-aluminum phase diagram showing the phases of interest to this study*

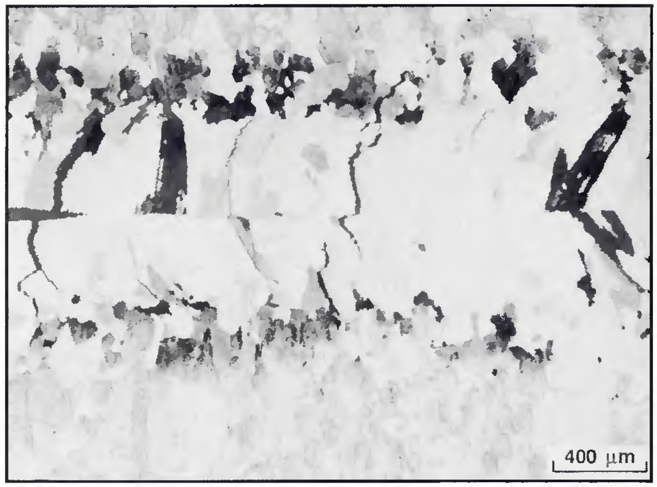


*Fig. 2—Optical micrograph showing a typical transverse crack in the $Fe_3Al$ alloy weldments*

4.2 to 8.4 mm/s (0.16 to 0.33 in./s).

Hot ductility testing was done on a Gleeble 1500 thermomechanical simulator. The specimen design used and the procedure are described elsewhere (Ref. 22). Weldment specimens were examined by light and electron metallographic techniques. The specimens for light microscopy were etched with a solution containing 40 mL $HNO_3$, 60 mL $CH_3COOH$, and 20 mL HCl. Specimens were prepared for transmission electron microscopy (TEM) by spark discharge machining 3-mm disks from the base material and the weld metal followed by electropolishing the disks in an electrolyte of one part nitric acid to four parts methanol in a Struers Tenupol jet polishing unit at −28°C (−18°F). TEM examinations were conducted using a Philips EM430.

## Results and Discussion

### Electron Beam Welding

Since past studies (Ref. 23) on ordered intermetallic alloys have shown that the high-energy beam process can produce successful welds owing to the highly concentrated heat source and possible grain refinement in the fusion zone structure, initial interest was focused on EB welding of iron aluminide alloys. The various Fe-Al alloys were EB welded at speeds ranging from 4.2 to 16.9 mm/s (0.2 to 0.7 in./s). After welding, the specimens were carefully examined for cracks using a low-magnification microscope. This was further confirmed using metallographic techniques. Table 2 summarizes the results of electron beam welding of $Fe_3Al$ as a function of the welding speed. In general, the results indicate that some $Fe_3Al$-based alloys can be successfully welded using the EB process. While the modified alloys (alloys containing Cr, Nb or Mn) did not exhibit any tendency to crack, the base alloys containing $TiB_2$ added for grain refinement (FA-41, FA-37, FA-39) did show a tendency to crack. Among these alloys, FA-41 and FA-37, although weldable at low welding speeds, showed severe cracking tendencies with increasing welding speed. The tendency for cracking at higher speeds is also consistent with the generation of a tear-drop-shaped weld pool that promotes coarse columnar grain structure within the fusion zone and promotes cracking. Further, a similar tendency to crack with increasing welding speeds has been observed during EB welding of $Ni_3Al$-based nickel aluminides (Ref. 23). The observed increase in weld cracking tendency with increasing welding speeds was attributed to the high heating and cooling rates and associated steep thermal gradients and stress that develop within the fusion zone and the heat-affected zone (Ref. 23). These factors may contribute to localization of stress that may exceed high-temperature fracture strength.

All of the EB welds made at the higher speeds in the base alloys showed intergranular cracks in the fusion zone with some of the cracks extending well into the base metal. Figure 2 shows a typical

**Table 1—Alloy Composition (at.-%)**

| Alloys | Heat | Al | Cr | Nb | Mn | B | $TiB_2$ | Fe |
|---|---|---|---|---|---|---|---|---|
| Base alloys | FA-41 | 27.0 | | | | | 1.0 | Bal. |
| | FA-37 | 28.0 | | | | | 1.0 | Bal. |
| | FA-61 | 28.0 | | | | | | Bal. |
| | FA-39 | 30.0 | | | | | 1.0 | Bal. |
| Cr modified alloys | FA-64 | 28.0 | 4.0 | | | | 1.0 | Bal. |
| | FA-72 | 28.0 | 4.0 | | | | | Bal. |
| Nb modified alloys | FA-66 | 28.0 | | 2.0 | | | 1.0 | Bal. |
| | FA-79 | 28.0 | | 1.0 | | | | Bal. |
| Mn modified alloy | FA-69 | 28.0 | | | 4.0 | | 1.0 | Bal. |
| Cr-Nb-B modified alloy(a) | FA-83 | 28.0 | | | | | | Bal. |

(a) For proprietary reasons, the actual composition has been omitted

**Table 2—EB Weldability**

| Alloys | Heat | Speed (mm/s) 4.2 | 8.5 | 16.9 |
|---|---|---|---|---|
| Base alloys | FA-41 | ● | ○ | ○ |
| | FA-37 | ● | ○ | ○ |
| | FA-61 | ● | ● | ● |
| | FA-39 | ○ | ○ | ○ |
| Cr modified alloys | FA-64 | ● | ● | ● |
| | FA-72 | ● | ● | ● |
| Nb modified alloys | FA-66 | ● | ● | ● |
| | FA-79 | ● | ● | ● |
| Mn modified alloy | FA-69 | ● | ● | ● |
| Cr-Nb-B modified alloy | FA-83 | ● | ● | ● |

●—No Cracks; ○—Cracks.

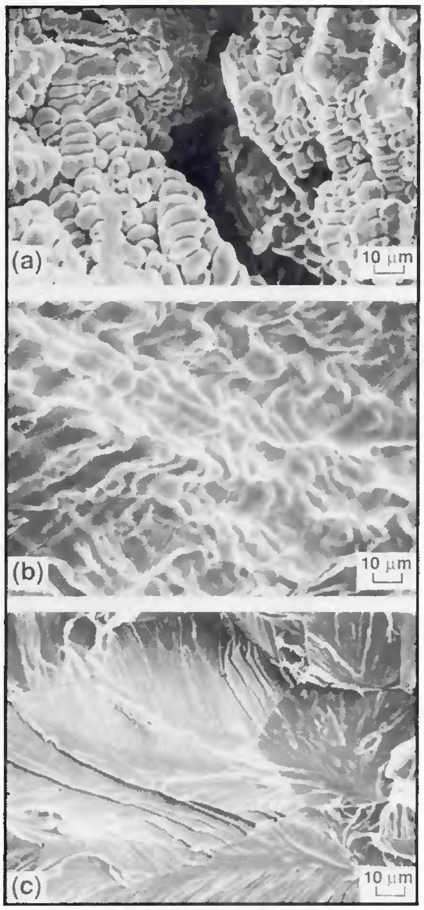


*Fig. 3 — Scanning electron micrographs of FA-37 cracked surface taken from: A — weld centerline; B — near the fusion line; C — the base material*

transverse crack in the $Fe_3Al$ alloy weldments. Scanning electron microscopic (SEM) examination of the cracked surface revealed the cracking in the fusion zone to be predominantly solidification cracking. Figure 3 shows a series of SEM photographs taken from the centerline of the fusion zone and into the heat-affected zone (HAZ). The cracked surface within the fusion zone is predominantly dendritic, indicating a hot crack — Figs. 3A and 3B. The possible dissociation of $TiB_2$ into Ti and B, as will be discussed later, could contribute to the formation of low melting liquid that may promote hot cracking. Both Ti and B are known to depress the melting point of iron. An SEM micrograph of a typical ruptured specimen in the base material is shown in Fig. 3C. As seen in Fig. 3C, the fracture mode in the base material is predominantly transgranular cleavage. This also indicates the lack of ductility in the base material that is typical of this alloy (Ref. 24).

Among the base alloys, only FA-61 without any $TiB_2$ addition could be successfully welded. In contrast, Alloy FA-39 welds cracked severely. This was somewhat surprising since Alloy FA-39 contained the highest aluminum content (30 at.-% Al) and an increase in aluminum content is known to increase the room-temperature ductility of the Fe-Al alloy (Ref. 24). However, it is pointed out that although FA-39 contained the highest aluminum content, it also contained $TiB_2$ additions, which seem to increase the cracking tendency of the welds as shown above. Furthermore, the increase in aluminum content significantly increases the thermal conductivity of the material. For example, considering the two alloys as a homogeneous mixture of iron and aluminum, the estimated thermal conductivity of Alloy FA-39 (51 W $mK^{-1}$) is approximately 13% more than Alloy FA-41 (45 W $mK^{-1}$). The increased thermal conductivity can increase the cooling rates, thus bringing the specimen into a temperature regime wherein the material is susceptible to cracking due to the lack of ductility. These factors, together with other metallurgical factors, may have contributed to the failure of the Alloy FA-39 weldments even at slowest welding speed.

In the ternary (Fe-Al-Cr, Fe-Al-Nb, Fe-Al-Mn) and other higher-order alloys, successful full-penetration EB welds were made for the full range of welding speeds investigated. Careful examination of the weld fusion zone and the heat-affected zone revealed no cracks in spite of the fact that some of these alloys contained 1.0 at.-% $TiB_2$, which was found to have a detrimental effect on the weldability of the binary Fe-Al alloys.

**Table 3—GTA Weldability**

| Alloys | Heat | Speed (mm/s) 4.2 | 8.5 |
|---|---|---|---|
| Base alloys | FA-41 | O | O |
| | FA-37 | O | O |
| | FA-61 | ● | ● |
| | FA-39 | O | O |
| Cr modified alloys | FA-64 | O | O |
| | FA-72 | ● | ● |
| Nb modified alloys | FA-66 | ● | ● |
| | FA-79 | ● | ● |
| Mn modified alloy | FA-69 | O | O |
| Cr-Nb-B modified alloy | FA-83 | O | O |

● — No Cracks; O — Cracks.

## Gas Tungsten Arc Welding

Table 3 summarizes the results of the GTA welding of $Fe_3Al$ as a function of welding speed for the different alloys considered in this investigation. The results confirm the deleterious effect of $TiB_2$ dispersion on the weldability of $Fe_3Al$ alloys, producing cracks along the weld centerline as shown in Fig. 4. Most of the modified alloys tested also experienced cracking with additions of $TiB_2$. However, in the absence of $TiB_2$, successful full-penetration welds were made on all the $Fe_3Al$ alloys except Alloy FA-83. Note that Alloy FA-66, containing niobium, did not exhibit any cracks even with additions of $TiB_2$, indicating that niobium is beneficial to the weldability of iron aluminides. Although Nb was added to improve elevated temperature properties of these alloys, the beneficial effect of Nb in preventing hot-cracking in these alloys is not known at present. The multicomponent alloy, FA-83, cracked upon welding. This was not expected since the alloying elements in FA-83, when used in a ternary alloy, were found to be extremely beneficial to the weldability of iron aluminides. Although boron has been found to improve the fabricability of iron aluminides, the results of the welding studies suggest that it is deleterious to the weldability. In general, the results indicate that

*Fig. 4 — Optical micrograph of FA-41 weldment showing a typical centerline crack in the fusion zone*

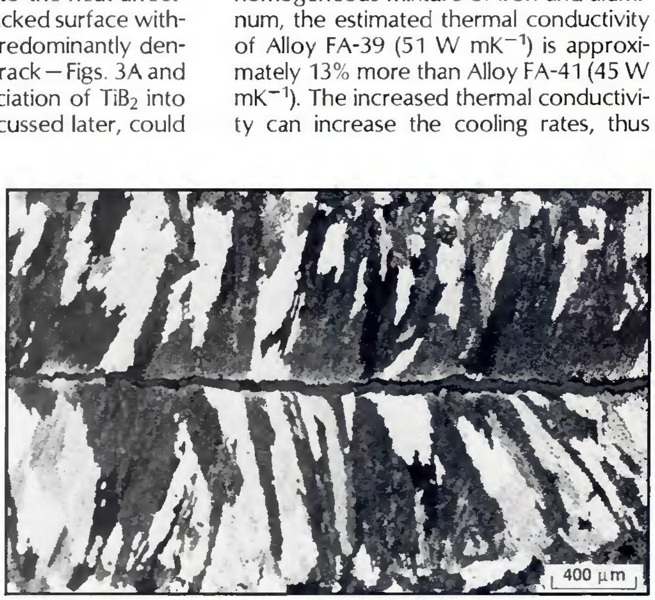

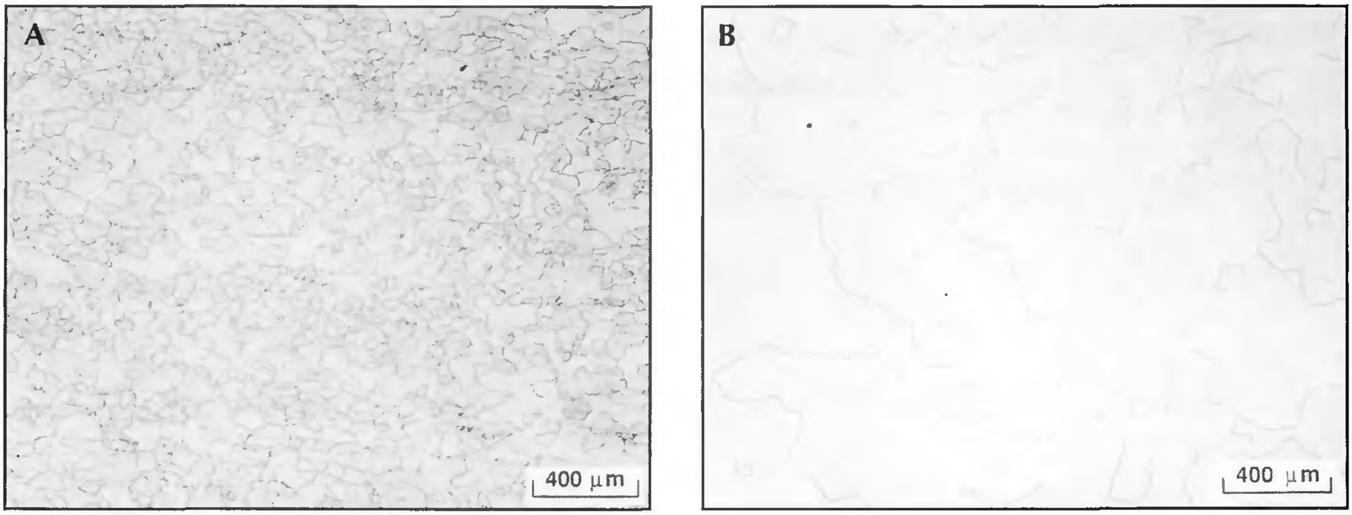


Fig. 5 — Typical recrystallized base metal microstructures of $Fe_3Al$ alloys. A — FA-41 with $TiB_2$ additions; B — FA-61 without $TiB_2$ additions

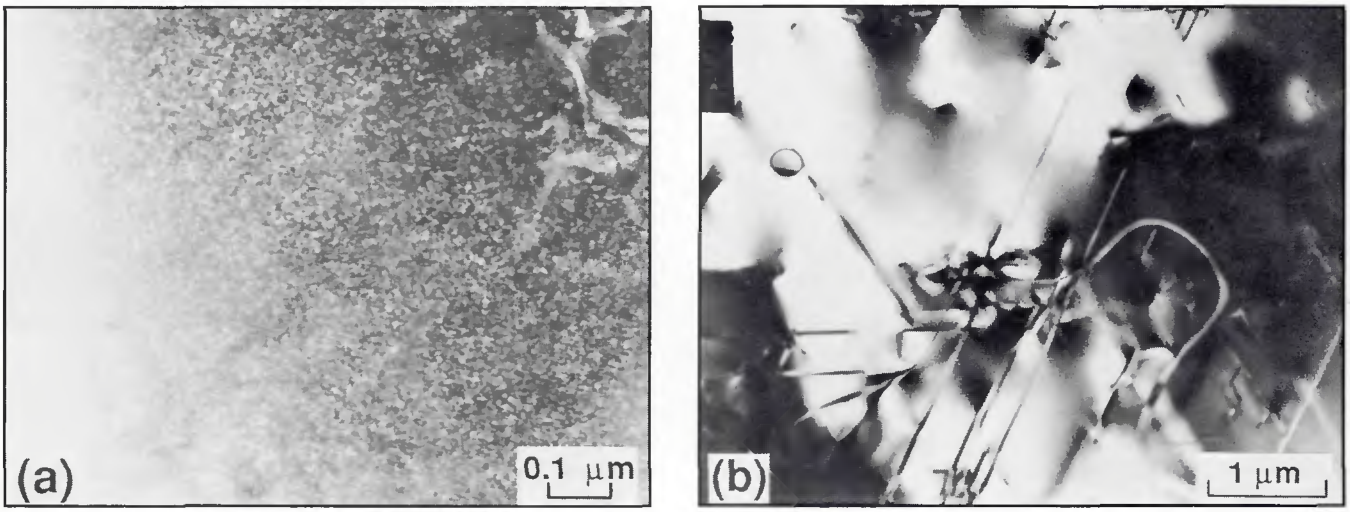


Fig. 6 — Transmission electron micrographs of $Fe_3Al$ alloys made using {111} superlattice reflections that show ordered $DO_3$ domains as bright areas. A — FA-79 base metal; B — FA-69 base metal

some $Fe_3Al$ alloys are weldable. Furthermore, the results clearly show that $TiB_2$ originally added to improve the low-temperature ductility and the high-temperature strength is deleterious to the weldability of the iron aluminides.

## Microstructures

### Base Metal

The typical recrystallized base metal microstructures of the Fe-Al alloys based on $Fe_3Al$ with and without $TiB_2$ additions are shown in Fig. 5. The base alloys containing $TiB_2$ added for grain refinement are FA-37, FA-39 and FA-41. These alloys had grain sizes of no larger than 50 $\mu$m, compared to the binary Alloy FA-61 without $TiB_2$, which had somewhat larger grains of up to 300 $\mu$m. The refinement in grain structure is mostly due to pinning of the grain boundaries by $TiB_2$. Chromium was added to the base alloy to improve the room-temperature ductility, while niobium or manganese were added to produce increased high-temperature strength. Chromium and manganese had little effect on the grain size. Chromium is reported to improve the room-temperature ductility by modifying the slip behavior and increasing the cleavage fracture strength (Refs. 25, 26).

Figure 6A shows a dark-field TEM image of unwelded Alloy FA-79 made with a {111} superlattice reflection that shows ordered $DO_3$ domains as bright areas. The domains are about 4 nm in diameter. The domain size is sensitive to composition and is a function of the heat treatment. For example, in Alloy FA-69 with the same heat treatment as FA-79, the $DO_3$ domains grew so large that a typical domain structure was not observed — Fig. 6.

### Fusion Zone

Figures 7 and 8 show typical EB weld fusion zone microstructures of two alloys, FA-64 and FA-72, wherein the former contains $TiB_2$ and the latter does not. Figures 9A and 9B are dark-field micrographs of the fusion zone of the same two alloys respectively, and show that the $DO_3$ domain structure is unaffected by the $TiB_2$ addition. The fusion zone microstructure of Alloy FA-64 contains coarse columnar grains. However, the size of these grains and the curvature depend to a large extent on the welding speed and the associated weld pool shape (Refs. 27, 28). The relationship between the pool shape and the grain structure is discussed elsewhere (Refs. 27, 28). In the fusion zone, the growth of the grains is predominantly epitaxial. It is surprising to see a columnar fusion zone structure in welds of alloys containing $TiB_2$ rather than fine equiaxed structure — Fig. 7. Apparently, $TiB_2$ in the alloy does not seem to act as an effective nucleating agent for the $Fe_3Al$ alloy. In Alloy FA-72 (without $TiB_2$) the fusion zone structure is much coarser — Fig. 8. However, this is

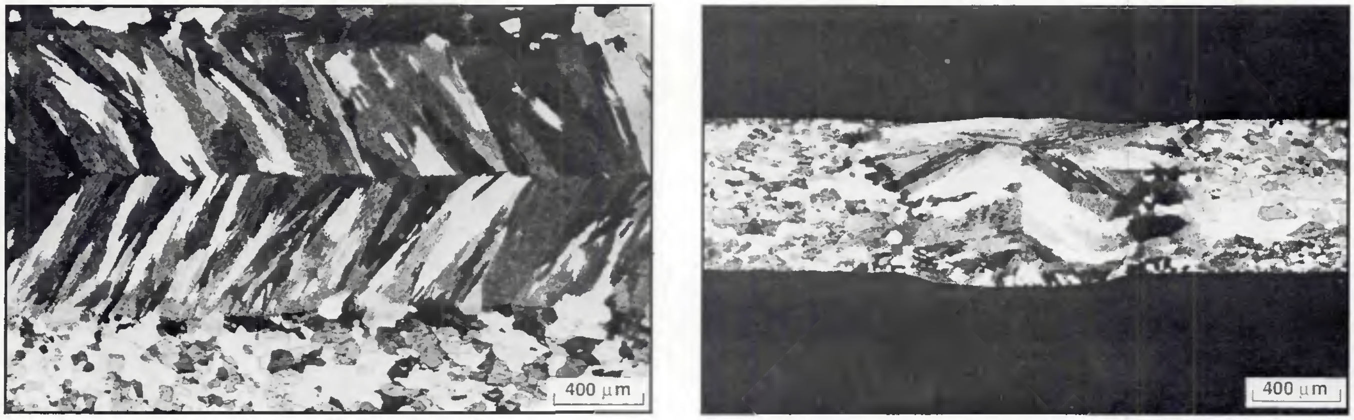


*Fig. 7 — Optical photomicrographs showing longitudinal and the transverse sections of the fusion zone of FA-64 alloy with $TiB_2$ addition*

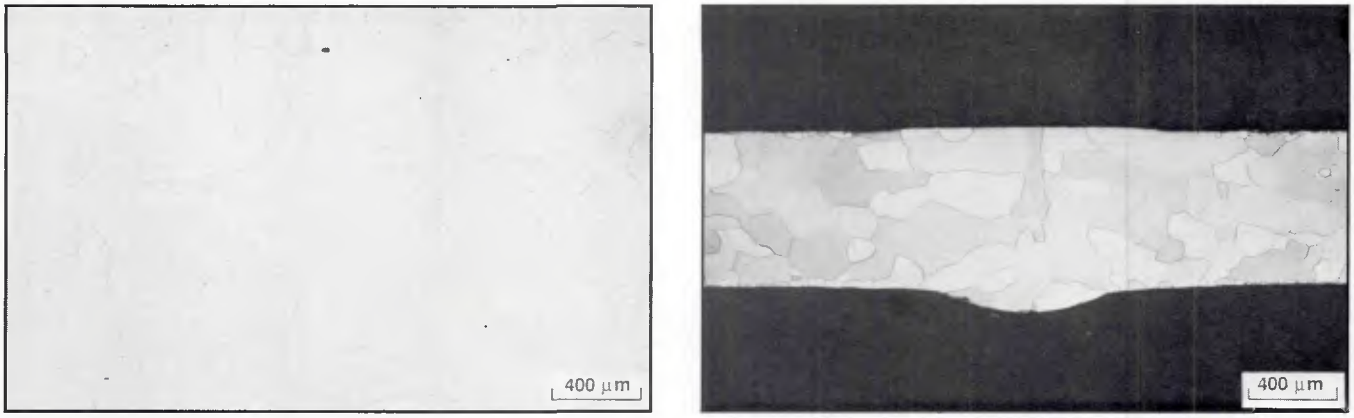


*Fig. 8 — Optical photomicrographs showing the longitudinal and the transverse sections of the fusion zone of FA-72 (without $TiB_2$ addition)*

mostly due to the coarse-grained base metal structure. Since most of the fusion zone structure develops by epitaxial growth of the grains near the fusion line, the base metal grain structure plays a significant role in determining the size of the fusion zone grains. It is pointed out that for all alloys the fusion zone structure of electron beam welds was much finer than the gas tungsten arc welds. The coarse grain structure of the GTA welds is one of the main reasons for greater incidence of cracking tendencies in the $Fe_3Al$ alloys during GTA welding compared to EB welds. Again, the relationship between grain structure and hot cracking tendency is well established in the literature (Ref. 27).

Figure 10 is a micrograph of the Alloy FA-72 EB weldment showing the fusion zone, the HAZ and the base metal. No significant grain coarsening due to welding was observed in the HAZ. A typical microhardness traverse across the weldment is also shown. A distinct feature of the hardness profile is that there is no significant change in the microhardness

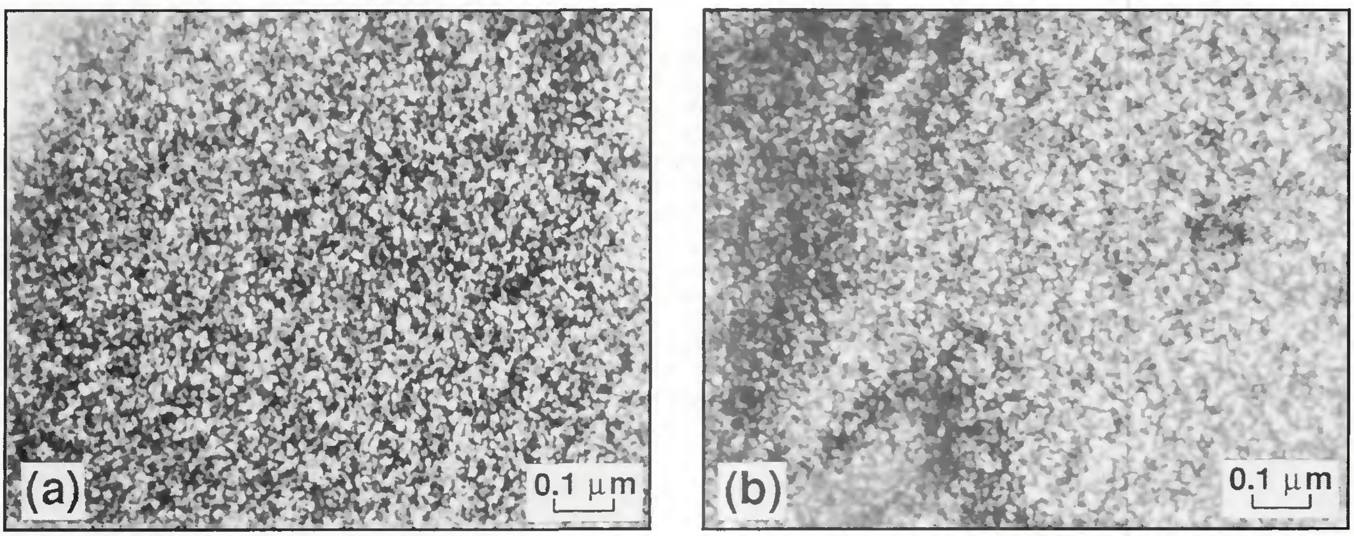


*Fig. 9 — Transmission electron micrographs of $Fe_3Al$ alloys made using {111} superlattice reflections that show ordered $DO_3$ domains as bright areas. A — FA-64 weld metal; B — FA-72 weld metal (both at 4.2 mm/s)*

value across the three zones. Previous work with other ordered intermetallic alloys such as (Fe, Ni)$_3$(V,Ti) have shown that the hardness significantly drops in the HAZ and the fusion zone (Ref. 29). This is attributed to the disordering transformation that the material undergoes at locations that experience temperatures above the critical temperature ($T_c$). Typically, there is insufficient time during cooling from a weld thermal cycle for the structure to reorder. However, in the present study the uniform hardness across the three zones seems to indicate that in the case of Fe-Al alloys the kinetics of the alloy going from ordered $DO_3$ structure to ordered B2 structure to disordered $\alpha$ and reverting back to $DO_3$ upon cooling in the weld metal, and the adjacent heat-affected zone is considerably faster. This was further confirmed by transmission electron microscopy of the weld metal and the adjacent HAZ.

Figure 11 shows the $DO_3$ domain structure in Alloys FA-69 and FA-79, using the {111} superlattice reflections. The domain size in the fusion zone of both alloys was 6 nm regardless of the fact that the base metal domains were small (4 nm) in FA-79 and were rather large in FA-69—Fig. 6B. Welding made no other difference in the microstructural features of these alloys. Figure 11 further compares the domain structure observed in FA-69 as a function of welding speed. The welding speed did not influence the domain size. The addition of chromium to the base $Fe_3Al$ alloy (Fig. 9A) doubled the $DO_3$ domain size to about 12 nm diameter after welding as compared to the alloys with additions of niobium or manganese—Figs. 11A and 11E.

### Effect of $TiB_2$ Addition

A recent study by Bordeau (Ref. 17) has shown that Fe-Al alloys containing $TiB_2$ particles could achieve room-temperature ductility of 15 to 20% (tensile elongation) with a tensile strength of 965 MPa (140 ksi). Therefore, considerable interest has been devoted to $Fe_3Al$-type Fe-Al alloys containing about 1.0 at.-% $TiB_2$. Although $TiB_2$ additions improve ductility and strength of $Fe_3Al$ alloys, it seems to have a deleterious effect on weldability.

The deleterious effect of $TiB_2$ on the weldability was more pronounced during GTA welding. All the alloys containing $TiB_2$ cracked, typically along the weld centerline. The only exception was Alloy FA-66, indicating that Nb is very beneficial to the weldability of the Fe-Al alloys. Figure 12 shows a typical centerline crack in the GTA fusion zone of Alloy FA-41. Secondary ion mass spectroscopy was performed to determine the distribution of $TiB_2$ in the base metal and along the crack and the possible effect it may have

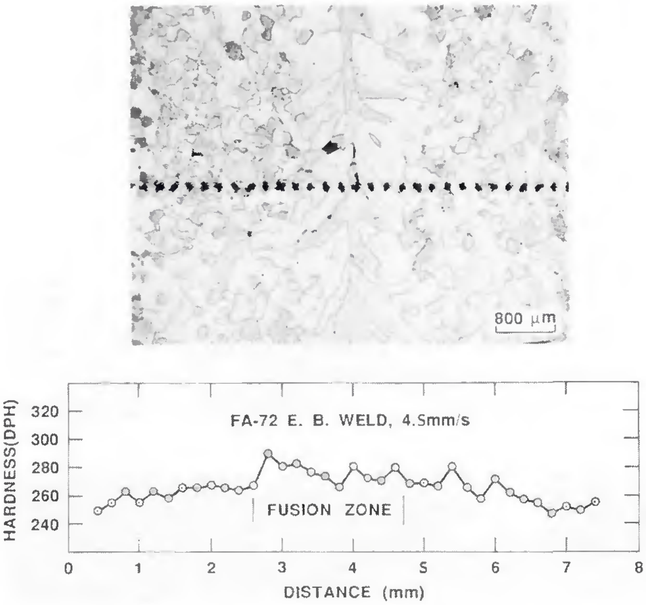


*Fig. 10—Micrograph of EB weldment of Alloy FA-72 showing fusion zone, HAZ and base metal. Also shown below is a typical microhardness traverse across the weldment*

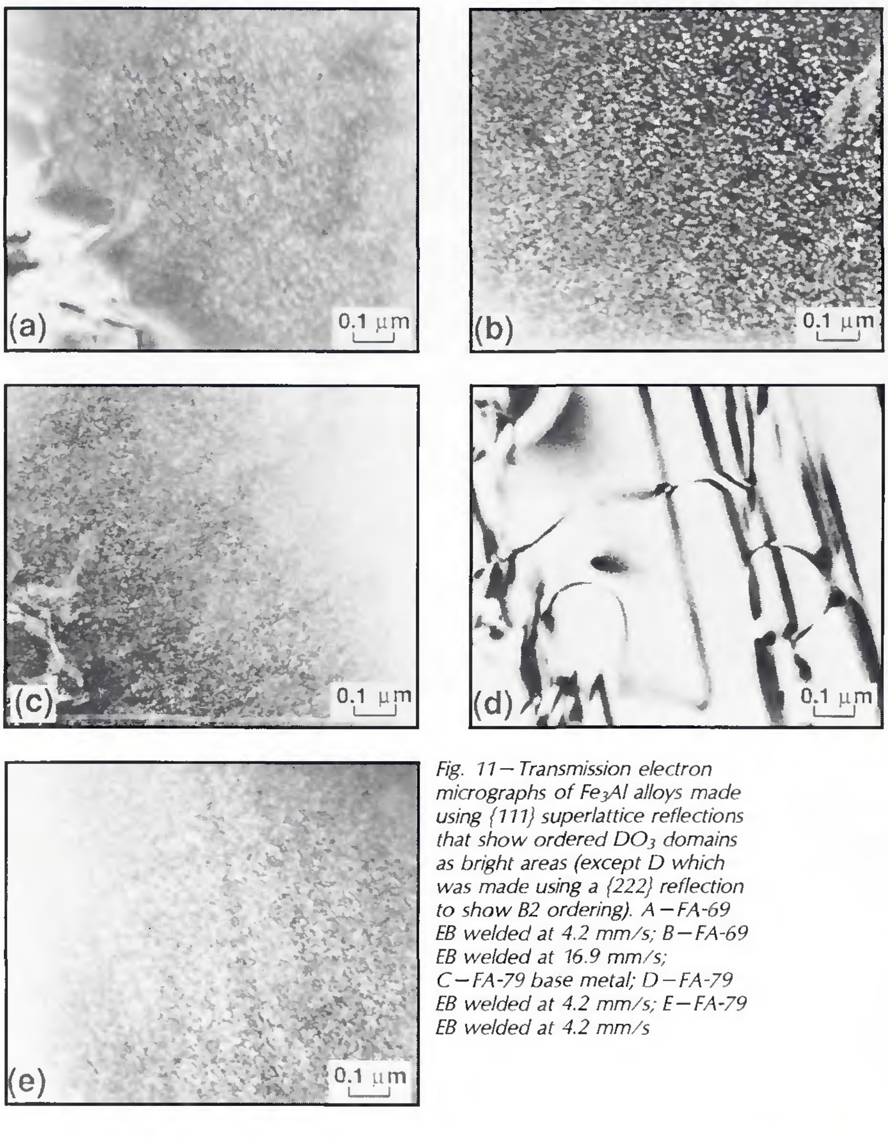


*Fig. 11—Transmission electron micrographs of $Fe_3Al$ alloys made using {111} superlattice reflections that show ordered $DO_3$ domains as bright areas (except D which was made using a {222} reflection to show B2 ordering). A—FA-69 EB welded at 4.2 mm/s; B—FA-69 EB welded at 16.9 mm/s; C—FA-79 base metal; D—FA-79 EB welded at 4.2 mm/s; E—FA-79 EB welded at 4.2 mm/s*

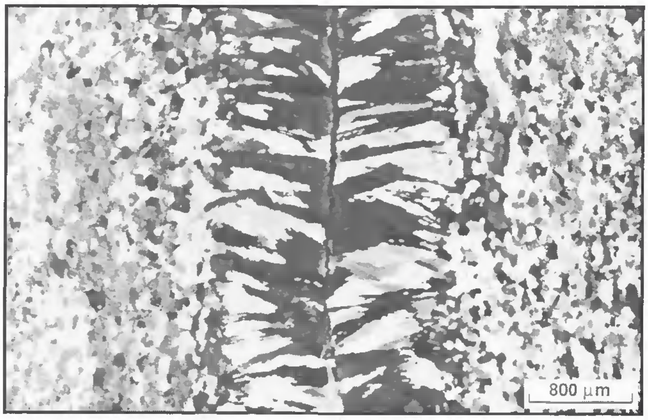


*Fig. 12 — Optical micrograph of FA-41 weldment showing a typical centerline crack in the fusion zone*

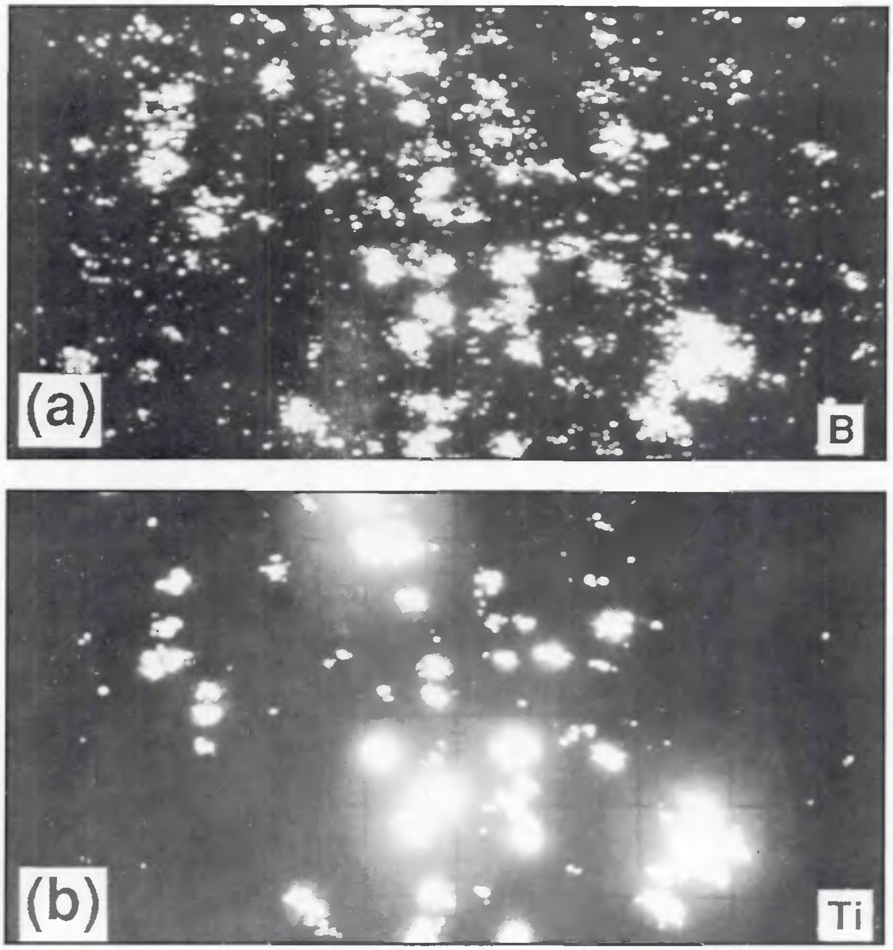


*Fig. 13 — SIMS. A — Boron; and B — titanium maps in the base metal of FA-41 shown in Fig. 12*


*Fig. 14 — SIMS boron map along the centerline crack shown in Fig. 12*

on the generation and subsequent propagation of the cracks. Figure 13 shows the boron and titanium maps in the base metal, indicating a uniform distribution of $TiB_2$. Such a distribution cannot explain the cracking observed in the fusion zone. Figure 14 shows the SIMS boron map at various locations in the fusion zone, along the centerline crack, showing a nonuniform distribution of $TiB_2$. The SIMS titanium map is similar. Notice the relatively large size $TiB_2$ particles at certain locations in the fusion zone, whereas at other locations the material is without any $TiB_2$. The results also show that the crack seems to have propagated along a region that is devoid of $TiB_2$ and along the interface between $TiB_2$ particles and the matrix.

Optical microscopy of the weld fusion zone revealed that the $TiB_2$ particles segregate preferentially to the grain and the solidification substructure boundaries — Fig. 15. The micrograph shows a nonuniform distribution of $TiB_2$ particles of varying size along the grain boundaries. Scanning electron microscopy of the crack surfaces further showed the segregation of $TiB_2$ particles to the interdendritic liquid — Fig. 16. These provide further evidence that $TiB_2$ does not act as an effective nucleation agent for refining the fusion zone structure. It is possible that the $TiB_2$ particles in the liquid melt may have dissociated at the temperature experienced during welding. The free


*Fig. 15 — Optical micrograph of the fusion zone structure showing $TiB_2$ distribution along the grain boundaries*

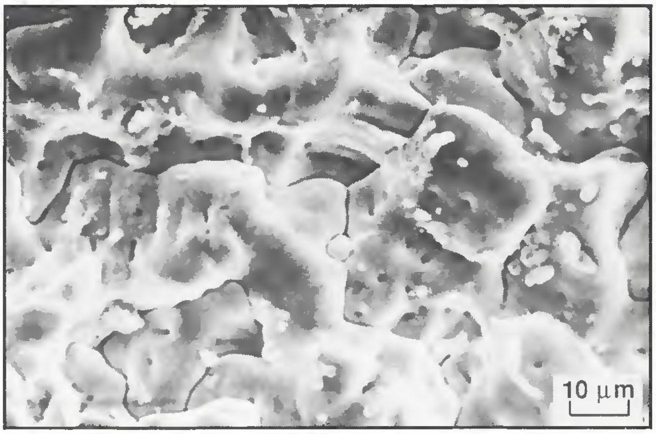


*Fig. 16 — Scanning electron micrograph of the crack surface showing $TiB_2$ particles at the interdendritic regions*

energy change associated with the dissociation reaction of $TiB_2$ can be calculated from thermodynamic considerations (Ref. 30). In order to simplify the calculation it is assumed that the molten metal in the weld pool is pure iron. For the dissociation of $TiB_2$,

$$\underline{Ti}B_2\ (s) = \underline{Ti}(in\ Fe) + 2\underline{B}(\text{in Fe})$$

the standard free energy $\Delta G°$ is,

$$\Delta G° = 29360 - 25.95\ T\ \text{cal/mole}$$

(Ref. 30)

where, the underline indicates that Ti and B are in solution in Fe. Typically, the temperature experienced by the liquid melt during welding is close to 2000°C (3632°F). At this temperature, the calculated large negative free energy change ($\approx -30{,}000$ cal/mole) for the reaction favors dissociation of $TiB_2$ to Ti(in Fe) and B(in Fe). During solidification of the weld, the solute (Ti and B) will segregate to the interdendritic region and can reform $TiB_2$ once again since thermodynamics favors this reaction as the temperature decreases. During solidification, these particles tend to be segregated along the grain boundaries and the interdendritic regions without acting as potent nucleating sites for new grains. This can explain the observed columnar dendritic structure in the weld metal. Typically, a potent nucleating agent promotes the formation of equiaxed grain structure. Since $TiB_2$ appears to be an ineffective nucleating agent for this alloy, it is likely that the bond at the interface between these particles and the matrix is not very strong. It is possible that the cracks may have initiated at these relatively weak locations and propagated during solidification as hot cracks. Figure 16 shows relatively large $TiB_2$ particles on the surface of the hot cracks.

**Hot Ductility**

Although the $Fe_3Al$ alloys investigated did not exhibit any HAZ cracking tendencies, the susceptibility of these alloys for HAZ cracking can be determined by a Gleeble hot ductility test. The test is based on the premise that the deformation behavior of a material during a given thermal cycle is indicative of its cracking tendency. The determination of the HAZ mechanical properties involved producing a microstructure in the Gleeble specimens typical of a portion of the HAZ of the weldment. Therefore, autogenous bead-on-plate welds were made on coupons of $Fe_3Al$, and the HAZ thermal cycles were measured using thermocouples located in the HAZ. Figure 17 shows the typical thermal cycle experienced by the weld HAZ during GTA welding at 4.2 mm/s (0.16 in./s).

During welding, the weld HAZ experiences temperatures far in excess of the transformation temperature between $DO_3$ and B2 (approximately 550°C/1022°F) and between B2 and the disordered $\alpha$ phase (approximately 750°C/1382°F) of the $Fe_3Al$ alloys. Therefore, an understanding of the mechanical behavior of the material in this temperature regime is particularly important to assess the behavior of the HAZ. The experimentally determined thermal cycle was imposed on the gauge section of the Gleeble specimen before testing at the preselected test temperature. Hot ductility was evaluated for Alloy FA-39 and Alloy FA-41 during the heating as well as during the cooling phase of the thermal cycle.

Figure 18 shows the on-heating hot ductility response of Alloys FA-39 and FA-41. The results show that the Fe-Al alloys possess excellent hot ductility at elevated temperatures. The ductility increases with an increase in temperature for both alloys. There was a sharp increase in the hot ductility with an increase in temperature beyond 550°C. The sharp increase in ductility beyond 550°C is likely due to the transformation from the ordered $DO_3$ structure to the ordered B2 structure at 550°C and finally to the disordered $\alpha$ phase beyond 750°C.

The results of the on-cooling hot ductility tests for Alloys FA-39 and FA-41 are presented in Fig. 19. The results once again confirm that the iron aluminides possess excellent hot ductility at elevated temperatures. The maximum observed ductility at 1100°C was found to be higher than that observed during the on-heating tests. The increased ductility is attributed to the longer exposure times at temperatures above 750°C (disordering temperature) allowing for the disordering

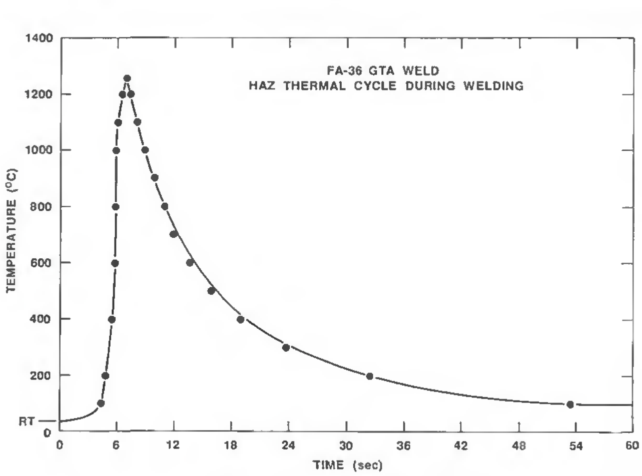


*Fig. 17 — Experimentally measured thermal cycle experienced by the weld HAZ during GTA welding at 4.2 mm/s*

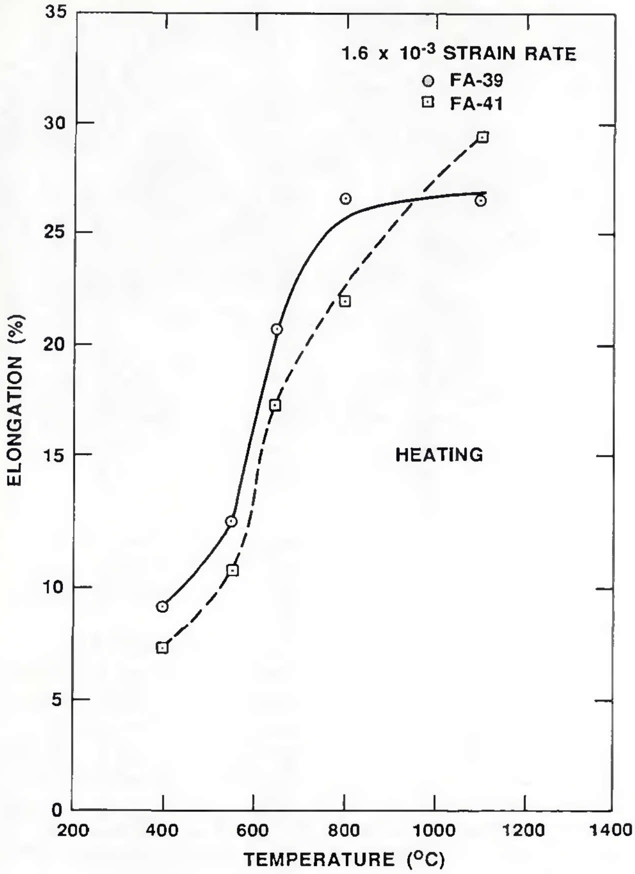


*Fig. 18 — On-heating hot-ductility response of Alloys FA-39 and FA-41*

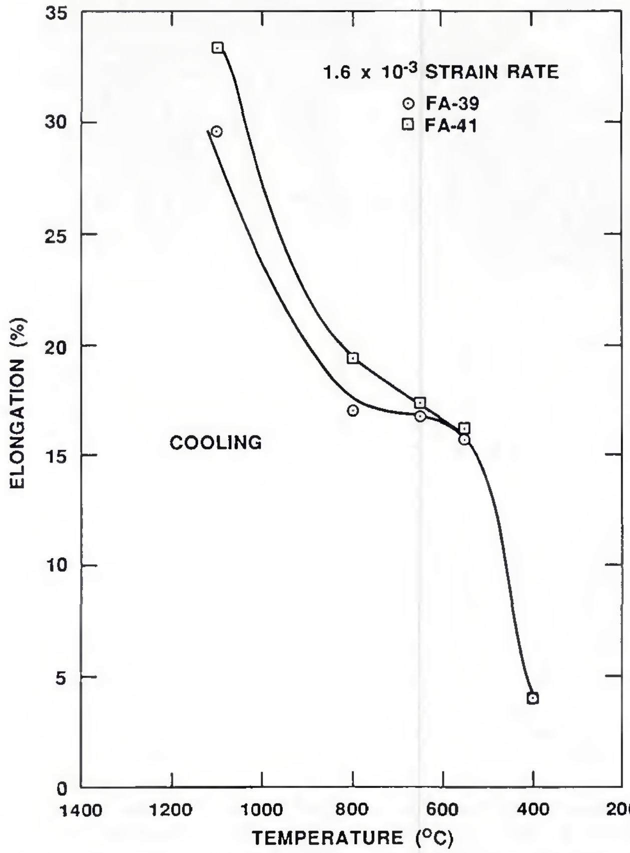


*Fig. 19 — On-cooling hot-ductility response of Alloys FA-39 and FA-41*

reaction to be complete. The ductility drops rapidly upon cooling from 1100°C (2012°F). Transmission electron microscopy of the iron aluminide weldments have already shown that the kinetics of ordering is very rapid in these alloys, and that the material reverts to a completely ordered structure upon cooling, with minimal growth in the domain size. The preprogrammed cooling rates from the peak temperature, based on the experimentally measured thermal cycle (Fig. 17), is relatively low (100°C/s — 180°F/s). At these low cooling rates, the material has ample time to reorder, resulting in the rapid reduction in the ductility.

Table 4 shows the static hot-tensile ductility results for the $Fe_3Al$ alloys (Ref. 24). These tests were performed in an Instron tensile testing machine at a strain rate of $3.3 \times 10^{-3}$ on specimens of 12.7-mm (0.5-in.) gauge length. The observed results from the Gleeble tests are lower than results of the static hot-tensile tests, which showed a sharp increase in ductility and an associated reduction in ultimate strength beyond 550°C. However, the static hot-tensile tests were performed using a strain rate of $3.3 \times 10^{-3}$ compared to a strain rate of $1.6 \times 10^{-3}$ for the Gleeble specimens, indicating that the alloy is strain rate sensitive.

**Table 4—Effect of Test Temperature on Tensile Properties of $Fe_3Al$**

| | Temp. (°C) | Yield Strength (MPa) | Ultimate Strength (MPa) | Elongation (%) |
|---|---|---|---|---|
| FA-41 | 20 | 483.3 | 830.16 | 2.8 |
| | 200 | 243.4 | 952.20 | 15.5 |
| | 400 | 237.9 | 828.78 | 21.0 |
| | 600 | 313.7 | 339.23 | 46.3 |
| | 700 | 160.0 | 165.48 | 60.3 |
| | 800 | 67.6 | 70.33 | 66.5 |
| FA-39 | 20 | 339.2 | 589.52 | 4.9 |
| | 200 | 270.3 | 919.79 | 19.8 |
| | 400 | 259.9 | 732.94 | 17.6 |
| | 600 | 322.0 | 430.94 | 42.8 |
| | 700 | 158.6 | 212.37 | 68.6 |
| | 800 | 88.3 | 109.63 | 93.6 |

## Summary

The results of the electron beam and gas tungsten arc welding of iron aluminides show that they are sometimes weldable using both welding processes. However, all the binary alloys and several of the ternary alloys experienced cracking either in the EB or GTA welds or in both when $TiB_2$ was present. The addition of $TiB_2$ did not act as an effective nucleation agent for refining the fusion zone structure. Thermodynamics favors dissociation of $TiB_2$ in the liquid melt at the temperatures experienced during welding. Upon solidification, Ti and B in the melt recombine to form $TiB_2$. During solidification, these particles tend to be segregated along the grain boundaries and the interdendritic region weakening the grain boundary cohesive strength. The SIMS boron and titanium maps showed that the cracks in the fusion zone propagated along the interface between $TiB_2$ and the matrix, as well as regions devoid of $TiB_2$.

There was no significant change in the hardness across the fusion zone, the HAZ and the base metal. Unlike $(Fe,Ni)_3(V,Ti)$

intermetallic alloy, in the case of iron aluminides, the fusion zone and adjacent HAZ reverted back to an ordered structure upon cooling from peak temperatures. Even though the domain size in the fusion zone was coarser than the base metal, welding did not have any significant effect on the microstructural features of these alloys. Hot ductility tests showed that iron aluminides are ductile at elevated temperatures. This would indicate a relatively crack-free HAZ, which was later confirmed upon welding.

*Acknowledgments*

The authors would like to thank M. Maguire of Colorado School of Mines and D. Easton of Oak Ridge National Laboratory for reviewing the manuscript. The research was supported by the U. S. Department of Energy, Morgantown Energy Technology Center, Surface Gasification of Materials Program and the Basic Energy Sciences Program, Division of Materials Sciences, U. S. Department of Energy, under contract DE-AC05-84OR21400 with Martin Marietta Energy Systems, Inc.

*References*

1. Stoloff, N. S., and Davies, R. G. 1966. The mechanical properties of ordered alloys. *Prog. Mater. Sci.* 13(1):1.
2. Kear, B. H., Sims, C. T., Stoloff, N. S., and Westbrook, J. H. Ordered alloys—structural applications and physical metallurgy. *Proceedings of the 3rd Bolton Landing Conference, September 1969,* Claitors, Baton Rouge, La.
3. Westbook, J. H. 1959. *Mechanical Properties of Intermetallic Compounds,* Wiley, New York, N.Y.
4. Westbrook, J. H. 1967. *Intermetallic Compounds,* Wiley, New York, N.Y.
5. Liu, C. T., and Inouye, H. 1979. Control of ordered structure and ductility of $(Fe,Co,Ni)_3V$ alloys. *Metall. Trans. A.* 10A: 1515.
6. Liu, C. T. 1984. Physical metallurgy and mechanical properties of ductile ordered alloys $(Fe,Co,Ni)_3V$. *Int. Metall. Rev.* 29:168.
7. Aoki, K., and Izumi, O. 1979. Improvement in room-temperature ductility of the $L1_2$ type intermetallic compound $Ni_3Al$ by boron addition. *Nippon Kinzoku Takkaishi* 43:1190.
8. Liu, C. T., and Koch, C. C. 1983. Development of ductile polycrystalline $Ni_3Al$ for high-temperature applications. *Proceedings of a Public Workshop on Trends in Critical Materials Requirements for Steels of the Future: Conservation and Substitution Technology for Chromium,* NBSIR-83-2679-2, National Institute of Standards and Technology, Washington, D.C.
9. Schulson, E. M., and Barker, D. R. 1983. A brittle to ductile transition in NiAl of a critical grain size. *Scr. Metall.* 17:519.
10. Inoue, A., Tomioka, H., and Masumoto, T. 1983. Microstructure and mechanical properties of rapidly quenched $L1_2$ alloys in Ni-Al-X systems. *Metall. Trans A.* 14A:1367.
11. Liu, C. T., White, C. L., Koch, C. C., and Lee, E. H. 1983. Preparation of ductile nickel aluminides for high-temperature use. *High-Temperature Materials Chemistry-II,* eds. L. A. Munir and D. Cubicciotti, Electro-chemical Society, Pennington, N.J., 83(7):21.
12. Taub, A. I., Huang, S. C., and Chang, K. M. 1984. Improved strength and ductility of $Ni_3Al$ by boron modification and rapid solidification. *Metall. Trans. A.* 15A:399.
13. Okamoto, H., and Beck, P. A. 1971. Phase relationships in the Fe- rich Fe-Al alloys. *Metall. Trans.* 2:569.
14. Oki, K., Hasaka, M., and Eguchi, T. 1973. Process of order-disorder transformations in Fe-Al alloys. *Jap. J. Appl. Phys.* 12(10):1522.
15. Horton, J. A., Liu, C. T., and Koch, C. C. 1984. *Proceedings of High-Temperature Alloys: Theory and Design,* Bethesda, Md., April 8–11, ed. J. O. Stiegler, TMS-AIME, p. 309.
16. Kerr, W. R. 1986. Fracture of $Fe_3Al$. *Metall. Trans.* 17A:2298.
17. Bordeau, R. G. 1987. Development of iron aluminides. *AFWAL-TR-87-4009,* Air Force Wright Aeronautical Laboratories, Wright-Patterson Air Force Base, Ohio, May.
18. Mendiratta, M. G., Ehlers, S. K., Dimiduk, D. M., Kerr, W. R., Mazdiyasni, S., and Lipsitt, H. A. 1987. A review of recent developments in iron aluminides. *High-Temperature Ordered Intermetallic Alloys, II,* Materials Research Society Symposia Proceedings, Vol. 81, eds. C. C. Koch, C. T. Liu, N. S. Stoloff, and O. Izumi, Materials Research Society, Pittsburgh, Pa. p. 393.
19. Diehm, R. S., and Mikkola, D. E. 1987. Effect of Mo and Ti additions on the high-temperature compressive properties of iron aluminides near $Fe_3Al$. *High-Temperature Ordered Intermetallic Alloys, II,* Materials Research Society Symposia Proceedings, Vol. 81, eds. C. C. Koch, C. T. Liu, N. S. Stoloff and O. Izumi, Materials Research Society, Pittsburgh, Pa. p. 329.
20. Culbertson, G., and Kortovich, C. S. 1986. Development of iron aluminides. *AFWAL-TR-85-4115,* Air Force Wright Aeronautical Laboratories, Wright-Patterson Air Force Base, Ohio, March.
21. McKamey, C. G., Liu, C. T., David, S. A., Horton, J. A., Pierce, D. H., and Campbell, J. J. 1988. Development of iron aluminides for gasification systems. *ORNL/TM-10793,* July.
22. Santella, M. L., and David, S. A. 1986. Weldability of $Ni_3Al$-type aluminide alloys. *Welding Journal* 65(5):129-s–137-s.
23. David, S. A., Jemian, W. A., Lui, C. T., and Horton, J. A. 1985. Welding and weldability of nickel-iron aluminides. *Welding Journal* 64(1):22-s–28-s.
24. McKamey, C. G., Liu, C. T., Cathcart, J. V., David, S. A., and Lee, E. H. 1986. Evaluation of mechanical and metallurgical properties of $Fe_3Al$-based aluminides. *ORNL/TM-10125,* September.
25. McKamey, C. G., Horton J. A., and Liu, C. T. 1988. Effect of chromium on room-temperature ductility and fracture mode in $Fe_3Al$. 1988. *Scripta Metall.* 22(10):1679.
26. McKamey, C. G., Horton, J. A., and Liu, C. T. 1988. unpublished research.
27. David, S. A., and Vitek, J. M. Correlation between solidification parameters and microstructures. To be published in *International Metals Review.*
28. David, S. A., and Liu, C. T. 1982. High-power laser and arc welding of thorium-doped iridium alloys. *Welding Journal* 61(5):157-s–163-s.
29. David, S. A., Braski, D. N., and Liu, C. T. 1986. Structure and properties of welded long-range-ordered alloys. *Welding Journal* 65(4):93-s–98-s.
30. Rao, Y. K. 1985. *Stoichiometry and Thermodynamics of Metallurgical Processes,* Cambridge University Press.